Sensitivity and Uncertainty in Matched-Filter-Based Gas Detection With Imaging Spectroscopy

Jay E. Fahlen, Philip G. Brodrick, Red Willow Coleman, Clayton D. Elder, David R. Thompson, *Senior Member, IEEE*, Andrew K. Thorpe, Robert O. Green, Joseph J. Green, Amanda M. Lopez, and Chuchu Xiang

***Abstract*— Recent advances in remote imaging spectroscopy have increased its utility for detecting and quantifying greenhouse gas emissions. In fact, multiple airborne and space-based instruments are actively used to estimate methane emissions. Many of these measurements are made using matched-filter-based detection and estimation algorithms. In this work, we present new methods for quantifying and improving the accuracy and uncertainty of these algorithms. Two new metrics are proposed that capture the biases and uncertainties in gas quantity measurements stemming from local surface and atmospheric variation, observation and solar geometries, and sensor noise. We show that one of these, termed the "sensitivity," can be used to correct the bias in the gas concentration length estimates due to variable atmospheres and backgrounds, reducing the estimator's root mean squared (rms) error in spectra that deviate from the mean spectrum. The second, termed the "uncertainty," represents the bias-removed statistical uncertainty in the corrected estimator. Expressions for the rms error both with and without the correction are provided along with interpretation to help quantify the various noise sources. The utility of the metrics is demonstrated using data from the Earth Surface Mineral Dust Source Investigation (EMIT) imaging spectrometer currently collecting Earth observations onboard the International Space Station (ISS). The EMIT data also demonstrates the potential accuracy increase afforded by the sensitivity correction over variable surface types. These metrics and their concomitant estimator accuracy increases could prove valuable for future work in quantifying gas source emission rates and their uncertainties, instrument design, and machine learning-based detection methods.**

***Index Terms*— Hyperspectral imaging, measurement uncertainty, satellite remote sensing, spectral matched filter.**

I. Introduction

In THE past decade, remote spectroscopic measurements of CH_4 point sources have rapidly advanced from simple proofs of concept to a mature technology used in emissions mitigation and regulatory assessment. In this approach, a remote instrument acquires a spectrum for each location in an image of the Earth's surface. Analysts interpret these spectra to look for an excess of CH_4 absorption, mapping plumes of gas enhancement that indicate emission source locations. Improvements in methodology, together with focused airborne campaigns and the increased availability of global imaging spectrometer data, are rapidly growing the catalog of remote CH_4 detections. As these technologies become more widespread, the demand for detecting smaller, subtler sources grows. To this end, it is critical to understand the uncertainties in the detection process—instrumental, environmental, and algorithmic. A rigorous understanding of uncertainty enables an observing system to confidently use a detection at the limit of statistical confidence rather than the much higher limit of visual ambiguity.

Remote CH_4 point source detection with imaging spectrometers was first demonstrated in [1]. The development of matched-filter detection approaches enabled more sensitive retrievals [2], [3] along with airborne campaigns that mapped hundreds of anthropogenic sources [5]. Controlled release experiments have demonstrated agreement between remotely sensed emissions and ground-measured flow rates [6]. The first facility-scale CH_4 detection was made from space using the Hyperion imaging spectrometer [7]. Following this, a Cambrian explosion of CH_4 surveys using commercial and agency platforms has occurred (e.g., [8], [9], [10], [11]). Large-scale airborne campaigns have quantified sectoral emissions over wide areas [12] and natural point sources have been detected [13], [14]. New spectrometers like one used on the Earth Surface Mineral Dust Source Investigation (EMIT) instrument onboard the International Space Station (ISS) have enabled large-scale surveys of emissions across multiple countries at a fidelity that supports comparisons against their reported emission estimates [11]. These remote CH_4 measurements have made the previously invisible CH_4 now visible in a way that allows for clearer emissions characterization and potential for informing mitigation strategies [15], [16], which is key to combating global climate change.

Below, we present two new metrics to help quantify CH_4 measurements performed with matched-filtering methods. These metrics include the effects of sensor and shot noise, local surface and atmospheric variation, and solar and look angle dependencies. Often overlooked, the metrics also include the change in performance due to variation in the background pixels used in the parameter estimation portion

Manuscript received 8 April 2024; revised 17 June 2024; accepted 27 July 2024. Date of publication 8 August 2024; date of current version 19 August 2024. This work was funded by the US Greenhouse Gas Center and by the National Aeronautics and Space Administration (NASA) Earth Science Division for greenhouse gas science and applications development. The Earth Surface Mineral Dust Source Investigation (EMIT) observations were funded as part of the NASA Earth Ventures-Instrument (EVI-4) Prime Mission. *(Corresponding author: Jay E. Fahlen.)*

Jay E. Fahlen, Philip G. Brodrick, Red Willow Coleman, David R. Thompson, Andrew K. Thorpe, Robert O. Green, Joseph J. Green, Amanda M. Lopez, and Chuchu Xiang are with the Jet Propulsion Laboratory, California Institute of Technology, Pasadena, CA 91011 USA (e-mail: jay.e.fahlen@jpl.nasa.gov).

Clayton D. Elder is with the Jet Propulsion Laboratory, California Institute of Technology, Pasadena, CA 91011 USA, and also with NASA Ames Research Center, Moffett Field, Mountain View, CA 94043 USA.

Digital Object Identifier 10.1109/TGRS.2024.3440174

of matched-filter-based detection methods. The first metric, termed "sensitivity," represents the tendency of the measurement to under- or over-estimate the methane in a pixel due to local variations in surface reflectivity or atmospheric transmission. Relative to the noise, more light is absorbed by a given methane plume over a bright surface than a dim one. Because the absorption mechanism is represented as a multiplicative factor on the radiance while matched filter detection methods rely on a spectral difference, pixels brighter than the mean in the relevant channels will overestimate methane while dimmer pixels underestimate. Because of this effect, the sensitivity described here is largely present due to the use of the matched filter. The second metric, simply "uncertainty," represents the statistical variation due to the same effects. Pixels bright in the relevant CH_4 channels will have a high signal-to-noise ratio (SNR) and low uncertainty while those that are dimmer will have a low SNR and high uncertainty. In contrast to the sensitivity, the uncertainty metric quantifies an inherent variation in the measurement due to sensor and shot noise that will be present in any estimation technique. The formula for the uncertainty given below, however, is specific to the estimator in use and will be different for different algorithms. Both of these metrics are demonstrated using methane gas data from the EMIT imaging spectrometer [17]. The metrics will apply equally to other gases, subject to the constraint that the atmospherically scattered light is small compared to the surface reflected light or otherwise compensated (see Section IV below for more detail).

We recognize that certain biases may still occur that are not included in the metrics described below. For example, pixels having no true methane present may be incorrectly biased to relatively large concentration lengths due to, among a variety of possibilities, confounding surface reflectivities (for example, [18] and figures below). Such false positives can occur even in regions having high sensitivity and low uncertainty. Nevertheless, the metrics help to provide confidence in the concentration length estimates and serve as a precursor product for further processing, including quantifying gas source emission rates.

II. Concentration Length Uncertainty

The sections below make use of the following simple fact regarding Gaussian random variables repeated here for ease of reading. Let $\mathbf{X}$ be a multivariate Gaussian random variable with mean $\boldsymbol{\mu}$ and covariance matrix $\mathbf{C}$, denoted by $\mathbf{X} \sim N(\boldsymbol{\mu}, \mathbf{C})$, where $\mathbf{X}$ and $\boldsymbol{\mu}$ are column vectors with length n and $\mathbf{C}$ is an $n \times n$ matrix. Then, $\mathbf{AX}+\mathbf{a} \sim N(\mathbf{A}\boldsymbol{\mu}+\mathbf{a}, \mathbf{ACA^T})$ for any vector $\mathbf{a}$ and matrix $\mathbf{A}$.

A. EMIT Signal Model

A simple model for EMIT's radiance measurements is

$$\mathbf{X} = e^{-\mathbf{a}l}\mathbf{L} + \mathbf{L_s} + \mathbf{n} \tag{1}$$

where $\mathbf{a}$ is the absorption coefficient in units of inverse meters, $\mathbf{L}$ is the radiance that has passed through a potential methane plume, $\mathbf{L_s}$ is the atmospherically scattered light that has not passed through the plume, and $\mathbf{n}$ is the sensor noise. The gas concentration length, sometimes termed "gas enhancement" or in this case the "CH_4 enhancement," represented as l is the concentration length of an intervening gas (like methane, for example) in parts-per-million meters (ppm m). As seen later, matched-filter methods estimate the gas quantity relative to that of the mean background, hence the term "enhancement." Boldface indicates a vector or matrix quantity; for example $\mathbf{a} = (a_0, a_1, \ldots, a_{N_s-1})$, where N_s is the number of spectral channels. In the following, $e^{-\mathbf{a}l}$, and its first order expansion term $-\mathbf{a}l$, is a vector that is multiplied by its neighbor element by element, which in this case is the radiance $\mathbf{L}$. The noise model $n \sim (\mathbf{0}, \boldsymbol{\Sigma})$ predicts both sensor noise and amplitude-dependent shot noise for a given radiance spectrum. For EMIT, the noise model was developed from laboratory measurements, refined using vicarious calibration experiments, and finally validated on both bright and dark surfaces. Details of the noise model and the validation process are found in recent work by Thompson et al. [17]. The EMIT sensor SNR varies by wavelength, but SNR ranges from 250 to over 500 in the methane absorption range for a typical bright soil surface under good illumination. The predicted noise covariance matrix $\boldsymbol{\Sigma}$ is diagonal because sensor noise is statistically independent in each channel. In principle, $\mathbf{n}$ also depends on the observed radiance, but for the purposes of this section, we will ignore that dependence. For a uniform scene, the radiance model $\mathbf{L}$ would be a constant vector, but for more realistic scenes it is a random variable. Making the simplifying assumption that it is a multivariate Gaussian random variable for the purposes of this discussion, we can model it as $\mathbf{L} \sim N(\boldsymbol{\mu}, \mathbf{C_L})$, where $\boldsymbol{\mu}$ is the mean radiance vector and $\mathbf{C_L}$ its covariance matrix. The relative importance of the scattered light component $\mathbf{L_s}$ depends on the wavelength region of interest. In this article, we are primarily focused on detecting methane in the short-wave infrared wavelength range of EMIT (2.1–2.5 μm) in which $\mathbf{L_s}$ is negligible, so we generally set it to 0 for the rest of this article. The results below are nevertheless applicable for other wavelength ranges or atmospheres in which it is possible to estimate and remove $\mathbf{L_s}$ through some other method, including the contributions from Rayleigh scattering in the near-infrared and from heavy aerosol loads [19].

As a result of these definitions, the radiance measurements are distributed as $\mathbf{X} \sim N(e^{-\mathbf{a}l}\boldsymbol{\mu}, \mathbf{ACA}^T)$, where $\mathbf{A}$ is the "absorption matrix" defined as $\mathrm{diag}(e^{-\mathbf{a}l})$. Under the H_0 hypothesis, $l \to 0$, $\mathbf{A}$ becomes the identity matrix, and $\mathbf{X} \sim N(\boldsymbol{\mu}, \mathbf{C_L} + \boldsymbol{\Sigma})$. The standard matched filtering algorithm assumes the mean and covariance estimates are formed under the assumption of H_0, so we use this as the basic distribution of the data

$$\mathbf{X} \sim N\left(e^{-\mathbf{a}l}\boldsymbol{\mu}, \mathbf{C_L} + \boldsymbol{\Sigma}\right). \tag{2}$$

B. EMIT Matched Filter and Maximum Likelihood Concentration Length Estimator

The standard matched filter is defined as $Y = \mathbf{s}^T\mathbf{C}^{-1}(\mathbf{X}-\boldsymbol{\mu})$, where $\mathbf{s} = -\mathbf{a}\boldsymbol{\mu}$ is the signal vector [3], [20]. As the matched filter is a unitless quantity, there is an implied concentration

length of 1 m in the definition of $\mathbf{s}$ that makes its units simply radiance. Given the signal model used above, $\mathbf{C} = \mathbf{C_L} + \mathbf{\Sigma}$. Accordingly, $Y \sim N(\mathbf{s}^T\mathbf{C}^{-1}[(e^{-\mathbf{a}l} - 1)\boldsymbol{\mu}], \mathbf{s}^T\mathbf{C}^{-1}\mathbf{s})$. Under the optically thin assumption

$$Y \sim N\big(l\,\mathbf{s}^T\mathbf{C}^{-1}(-\mathbf{a}\boldsymbol{\mu}), \mathbf{s}^T\mathbf{C}^{-1}\mathbf{s}\big). \tag{3}$$

Note that although the term in parenthesis in the mean of Y appears to be the same as in the definition of $\mathbf{s}$, there is no implied concentration length so that the mean of Y is unitless, as expected. Nevertheless, the value is numerically equivalent so for convenience we refer to both quantities as $\mathbf{s}$ and therefore rewrite the distribution as

$$Y \sim N\big(l\,\mathbf{s}^T\mathbf{C}^{-1}\mathbf{s}, \mathbf{s}^T\mathbf{C}^{-1}\mathbf{s}\big) \tag{4}$$

keeping in mind that the units will be ambiguous with this notation.

An estimator for the concentration length can be determined intuitively by simply taking Y and dividing by its variance, as can be seen by examining Y's mean value. It turns out that this is in fact the maximum likelihood estimator (MLE) of the concentration length

$$\hat{l} \equiv \frac{\mathbf{s}^T\mathbf{C}^{-1}(\mathbf{X} - \boldsymbol{\mu})}{\mathbf{s}^T\mathbf{C}^{-1}\mathbf{s}} \tag{5}$$

whose distribution can be obtained from inspection of Y's distribution as

$$\hat{l} \sim N\left(l, \frac{1}{\mathbf{s}^T\mathbf{C}^{-1}\mathbf{s}}\right). \tag{6}$$

EMIT's standard concentration length estimates are produced using this MLE and it forms the basis for the uncertainty calculation below.

C. Concentration Length Sensitivity and Uncertainty

The MLE concentration length estimate whose distribution is shown in (6) is unbiased in the sense that the mean is the true concentration length provided the mean is computed over the full distribution of backgrounds ($\boldsymbol{C_L} \neq \mathbf{0}$). Similarly, the global uncertainty is provided by the variance component. However, any individual spectrum deviates from the mean spectrum, yielding a bias in the estimate and a change in the variation. To calculate these, we create a new signal model that represents a test spectrum to show the relative change to the mean, as in

$$\mathbf{X} = e^{-\mathbf{a}l}\boldsymbol{\kappa}\boldsymbol{\mu} + \mathbf{n}(\boldsymbol{\kappa}\boldsymbol{\mu}) \tag{7}$$

where expressions involving the vector $\boldsymbol{\kappa}$ are to be interpreted as element-by-element products and $\boldsymbol{\kappa} = \mathbf{L}/\boldsymbol{\mu}$. This choice of definition for $\boldsymbol{\kappa}$ simplifies interpretation by showing the deviation of the test spectrum relative to the mean. The noise term here represents the combination of electronic sensor noise and signal-dependent shot noise. Below, we substitute EMIT's noise model so that $\mathbf{n}(\boldsymbol{\kappa}\boldsymbol{\mu}) \sim N(\mathbf{0}, \mathbf{\Sigma}(\boldsymbol{\kappa}\boldsymbol{\mu}))$, where $\mathbf{\Sigma}(\boldsymbol{\kappa}\boldsymbol{\mu})$ is a diagonal matrix whose elements are determined by the sensor noise model and the test spectrum's radiance. Thus, the signal model used in this section represents repeated measurements of the same scene with the solar and look geometries fixed. Inserting into (5), using the optically-thin assumption, and rearranging terms yields the distribution of the MLE given by

$$\hat{l} \sim N\left(\frac{\mathbf{s}^T\mathbf{C}^{-1}(\boldsymbol{\kappa} - 1)\boldsymbol{\mu}}{\mathbf{s}^T\mathbf{C}^{-1}\mathbf{s}} + \frac{\mathbf{s}^T\mathbf{C}^{-1}\boldsymbol{\kappa}\mathbf{s}}{\mathbf{s}^T\mathbf{C}^{-1}\mathbf{s}}l, \frac{\mathbf{s}^T\mathbf{C}^{-1}\mathbf{\Sigma}(\boldsymbol{\kappa}\boldsymbol{\mu})\mathbf{C}^{-1}\mathbf{s}}{\left(\mathbf{s}^T\mathbf{C}^{-1}\mathbf{s}\right)^2}\right). \tag{8}$$

The first term of the mean is independent of the true methane quantity l and represents the tendency toward bias (false alarms) as the test spectrum deviates from the mean ($\boldsymbol{\kappa} \neq \mathbf{1}$). The second term represents the change to $\hat{l}$ as a function of the true methane quantity. The scale factor $(\mathbf{s}^T\mathbf{C}^{-1}\boldsymbol{\kappa}\mathbf{s})/(\mathbf{s}^T\mathbf{C}^{-1}\mathbf{s})$ applied to l determines the sensitivity of the measurement to the true methane quantity. The sensitivity tends to 1 as the radiance spectrum approaches the mean spectrum and deviates depending on the individual spectrum. A major component of the variation is due to the overall brightness (the magnitude of $\boldsymbol{\kappa}$) as can be seen by replacing $\boldsymbol{\kappa}$ with a scaling of the mean spectrum. In this case, $\boldsymbol{\kappa} \to \kappa$ and the sensitivity $(\mathbf{s}^T\mathbf{C}^{-1}\boldsymbol{\kappa}\mathbf{s})/(\mathbf{s}^T\mathbf{C}^{-1}\mathbf{s}) \to \kappa$, showing that the estimated methane quantity in a test spectrum is biased with the radiance deviation from the mean.

The bias in the estimate due to the radiance can be corrected by dividing the sensitivity out of the estimator, resulting in

$$\hat{l}_c = \left(\frac{\mathbf{s}^T\mathbf{C}^{-1}\boldsymbol{\kappa}\mathbf{s}}{\mathbf{s}^T\mathbf{C}^{-1}\mathbf{s}}\right)^{-1}\hat{l} \sim N\left(\frac{\mathbf{s}^T\mathbf{C}^{-1}(\boldsymbol{\kappa} - 1)\boldsymbol{\mu}}{\mathbf{s}^T\mathbf{C}^{-1}\boldsymbol{\kappa}\mathbf{s}} + l, \frac{\mathbf{s}^T\mathbf{C}^{-1}\mathbf{\Sigma}(\boldsymbol{\kappa}\boldsymbol{\mu})\mathbf{C}^{-1}\mathbf{s}}{\left(\mathbf{s}^T\mathbf{C}^{-1}\boldsymbol{\kappa}\mathbf{s}\right)^2}\right). \tag{9}$$

As seen in the second term of the mean, the scaling to the concentration length is removed, but that advantage comes at the cost of inflating the variance at low radiance levels. To better understand the differences, we compute the root mean squared (rms) error $\langle(\hat{l} - l)^2\rangle^{1/2}$. Recognizing the right side as the square root of the mean of a noncentral chi-squared random variable with one degree of freedom, we compute the squared rms for both the original MLE and the corrected version as

$$\left\langle\left(\hat{l} - l\right)^2\right\rangle = \frac{\mathbf{s}^T\mathbf{C}^{-1}\mathbf{\Sigma}(\boldsymbol{\kappa}\boldsymbol{\mu})\mathbf{C}^{-1}\mathbf{s}}{\left(\mathbf{s}^T\mathbf{C}^{-1}\mathbf{s}\right)^2} + \left(\frac{\mathbf{s}^T\mathbf{C}^{-1}(\boldsymbol{\kappa} - 1)\boldsymbol{\mu}}{\mathbf{s}^T\mathbf{C}^{-1}\mathbf{s}} + \left(\frac{\mathbf{s}^T\mathbf{C}^{-1}\boldsymbol{\kappa}\mathbf{s}}{\mathbf{s}^T\mathbf{C}^{-1}\mathbf{s}} - 1\right)l\right)^2 \tag{10}$$

and

$$\left\langle\left(\hat{l}_c - l\right)^2\right\rangle = \frac{\mathbf{s}^T\mathbf{C}^{-1}\mathbf{\Sigma}(\boldsymbol{\kappa}\boldsymbol{\mu})\mathbf{C}^{-1}\mathbf{s}}{\left(\mathbf{s}^T\mathbf{C}^{-1}\boldsymbol{\kappa}\mathbf{s}\right)^2} + \left(\frac{\mathbf{s}^T\mathbf{C}^{-1}(\boldsymbol{\kappa} - 1)\boldsymbol{\mu}}{\mathbf{s}^T\mathbf{C}^{-1}\boldsymbol{\kappa}\mathbf{s}}\right)^2. \tag{11}$$

As $\kappa \to 1$, both expressions reduce to the same value showing that the differences only occur due to the test spectrum deviating from the mean. In addition, in a uniform scene both $\kappa \to 1$ and $C \to \mathbf{\Sigma}(\boldsymbol{\kappa}\boldsymbol{\mu})$, leaving both expressions equal and equivalent to the variance term in (6). It is instructive to consider each term separately. The first term for both represents the fundamental statistical noise floor, which increases

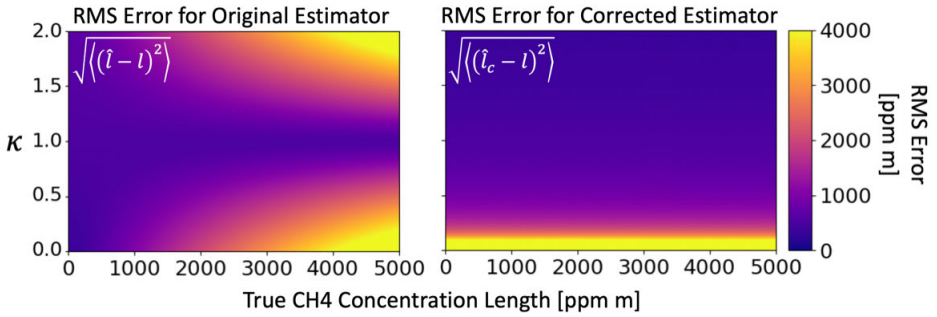

Fig. 1. RMS error for a typical $\boldsymbol{\mu}$ and $\mathbf{C}$ and using EMIT's noise model for $\boldsymbol{\Sigma}(\boldsymbol{\kappa\mu})$. In both figures κ is a scalar that simply scales the mean spectrum. (Left) corresponds to (10) and (right) corresponds to (11), representing the rms difference between the estimated concentration length and the true value.

with the radiance (κ) following shot noise in the original MLE. The corrected estimator, on the other hand, shows the opposite behavior, with the statistical error increasing at lower radiance ($\kappa \to 0$) as mentioned previously. The error for both estimators then increases due to two possible biases. The first bias occurs in both versions and represents the tendency of the surface reflectivity and the atmospheric absorption to occasionally mimic the CH_4 signal, driving false alarms. The second bias occurs for $\boldsymbol{\kappa} \neq 1$ and $l \neq 0$; it is removed in the corrected estimator. Both expressions are plotted for typical values of the mean and covariance in Fig. 1. The rms error of the original uncorrected MLE is symmetric about $\kappa = 1$ and becomes large as κ deviates from 1. The corrected estimator's rms error shows no dependence on concentration length, as expected. In addition, for $\kappa > 1$ and for much of the $\kappa < 1$ region at larger concentration lengths, the rms error of the corrected estimator is smaller than that of the original. Since most observed plumes are in this region of parameter space, the corrected estimator is generally more accurate than the original.

These results suggest a more nuanced interpretation of the original MLE. As shown in (6), $\hat{l}$ is unbiased when averaged over the entirety of the radiance variation, but it yields a biased estimate in any individual spectrum in which CH_4 is present but whose radiance deviates from that of the mean spectrum. It is possible to remove this bias using the ad hoc scaling by the sensitivity used in the corrected MLE but at the cost of increasing the statistical and surface/atmospheric portions of the rms error for certain deviations from the mean spectrum, particularly for low radiance or those deviations that mimic the CH_4 absorption spectrum. Accordingly, we do not recommend replacing the original MLE for wide area searches for CH_4 but rather using the corrected estimator to improve the quantification of plumes detected with the original MLE.

We propose two new metrics: the sensitivity and the uncertainty. These are based on the expressions above, but recognize that in real data, we cannot separate the bias terms, nor do we have access to either the noise-free radiance $\boldsymbol{\kappa\mu}$ or to that quantity without the potential presence of CH_4. Instead, we replace $\boldsymbol{\kappa}$ with $\hat{\boldsymbol{\kappa}} = \mathbf{X}/\boldsymbol{\mu}$, where $\mathbf{X}$ is the measured spectrum. The sensitivity is then defined as

$$S \equiv \frac{\mathbf{s}^T\mathbf{C}^{-1}\hat{\boldsymbol{\kappa}}\mathbf{s}}{\mathbf{s}^T\mathbf{C}^{-1}\mathbf{s}} \tag{12}$$

while the uncertainty is

$$U^2 \equiv \frac{\mathbf{s}^T\mathbf{C}^{-1}\boldsymbol{\Sigma}\left(\hat{\boldsymbol{\kappa}}\boldsymbol{\mu}\right)\mathbf{C}^{-1}\mathbf{s}}{\left(\mathbf{s}^T\mathbf{C}^{-1}\hat{\boldsymbol{\kappa}}\mathbf{s}\right)^2}. \tag{13}$$

III. Uncertainty Estimates for EMIT

To illustrate the behavior of the sensitivity S and uncertainty U, we present both from a typical EMIT scene. Fig. 2 shows an RGB representation of the radiance, $\hat{l}$, S, and U for EMIT scene emit20231008t161127 in which there is no apparent CH_4 detection. Note that in all figures showing EMIT data, pixels flagged as having clouds or surface water have been replaced by null values. The circular fields demonstrate the various terms in (10) with specific examples indicated by the colored arrows. The green and orange arrows show locations with relatively high and low, respectively, radiance and sensitivity. The uncertainty behaves oppositely. Neither of the regions' spectral deviations from the mean appears to drive surface or atmospheric biases, as seen in the second plot showing $\hat{l}$. The blue region, on the other hand, shows near-nominal sensitivity (near 1) with relatively low uncertainty, but here the surface does drive an apparent bias in $\hat{l}$. There is no apparent true CH_4 plume in these images, but were one to span the scene, we would expect strong biases in $\hat{l}$ following the sensitivity.

Figs. 3–5 show an example EMIT scene in which a CH_4 plume does appear to be modulated by the surface sensitivity. The plume, whose approximate boundary is shown in white or black lines, is emitted at the lower right and carried to the upper left by the wind (it is likely that the plume is actually emitted from the small, high-sensitivity spot in which vegetation has been removed at (cross, along) track pixel (562, 1793) next to the diagonally-cutting road). The apparent plume passes from the vegetated region surrounding the point of emission along and into a more reflective region toward the upper left. In the dimmer vegetated region, the sensitivity is low and the uncertainty high. We thus expect the plume concentration length to be underestimated here. Conversely, the sensitivity is high and the uncertainty low in the brighter region with the plume being overestimated there. The bias in the estimate can be seen in the uncorrected concentration length map on the left side of Fig. 4 where the stronger parts of the plume appear to follow the local surface variation. The corrected version on the right side shows less dependence on

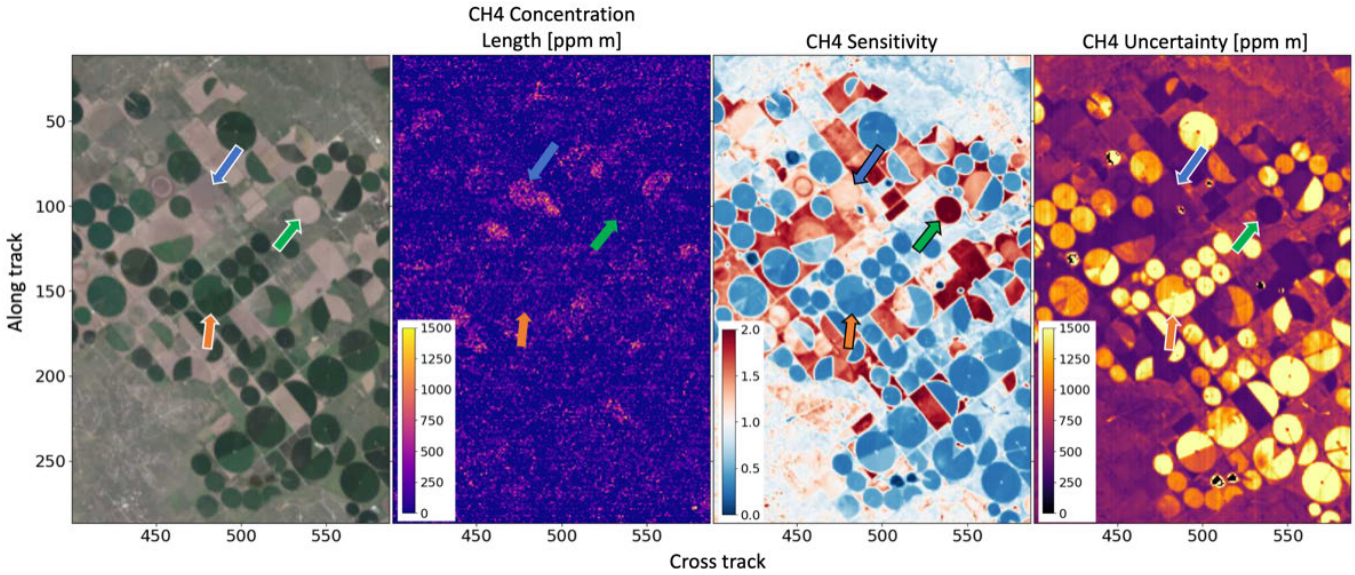

Fig. 2. From (left) RGB of radiance, estimated CH_4 concentration length $\hat{l}$, CH_4 sensitivity S, and CH_4 uncertainty U for EMIT scene emit20230817t201510. The green arrow highlights a location with high radiance and low sensitivity, the orange arrow shows a region with low radiance and high sensitivity, and the blue arrow shows an area where the sensitivity is nominal but there is an apparent bias in the concentration length.

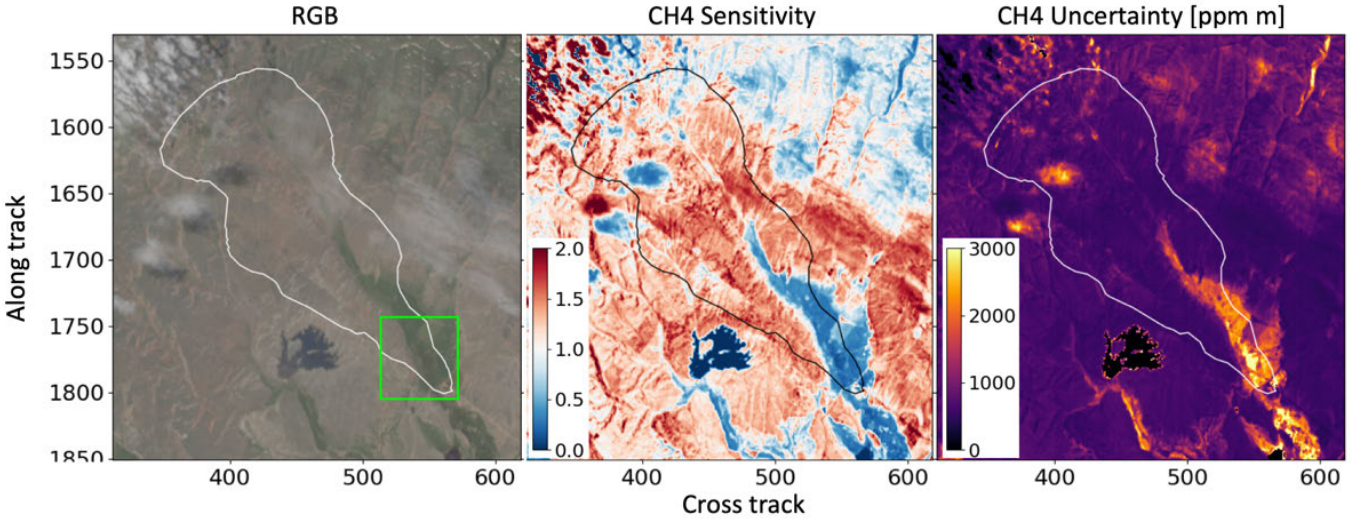

Fig. 3. From (left) RGB image of EMIT scene emit20230612t162103, CH_4 sensitivity S, and CH_4 uncertainty U. The green box represents the region shown in Fig. 5.

the local surface, as expected. These effects are seen more clearly in the zoomed-in view panels of Fig. 5. The uncertainty metric is useful here as its value captures the apparent spatial variation in concentration length in the corrected estimate.

Figs. 6 and 7 show a second example of an apparent plume. The emission source appears to be at the right edge of the delineated plume boundary in a location cleared of vegetation having high sensitivity. Shortly downwind the local terrain shifts to a low-sensitivity vegetated region. Further downwind the terrain again shifts to a higher sensitivity region. These changes are apparent in the concentration length shown on the left side of Fig. 7. The correction, shown at right, removes much of the plume's apparent dependence on the local surface. However, by reducing the measured concentration length's dependence on the surface, the correction also inflates both the statistical uncertainty and, evidently, the tendency of some pixels outside of the plume to yield false alarms. This is consistent with the effects of the correction on the rms error, specifically the second term in (11) when $\kappa < 1$.

To better see the challenge in distinguishing the background bias from a true methane observation [second versus third term in (10)], Fig. 8 shows a simple simulated plume injected into the background matched filter detections from an EMIT data scene. The simulated plume is a simple Gaussian plume as defined in, for example, [21, eq. (3)]. The plume parameters were chosen arbitrarily to generate a visually realistic plume. The figure shows the sensitivity S in the upper left and the uncorrected concentration length estimate in the bottom left. The other two vertical pairs of panels show the simulated plume in the top panel added

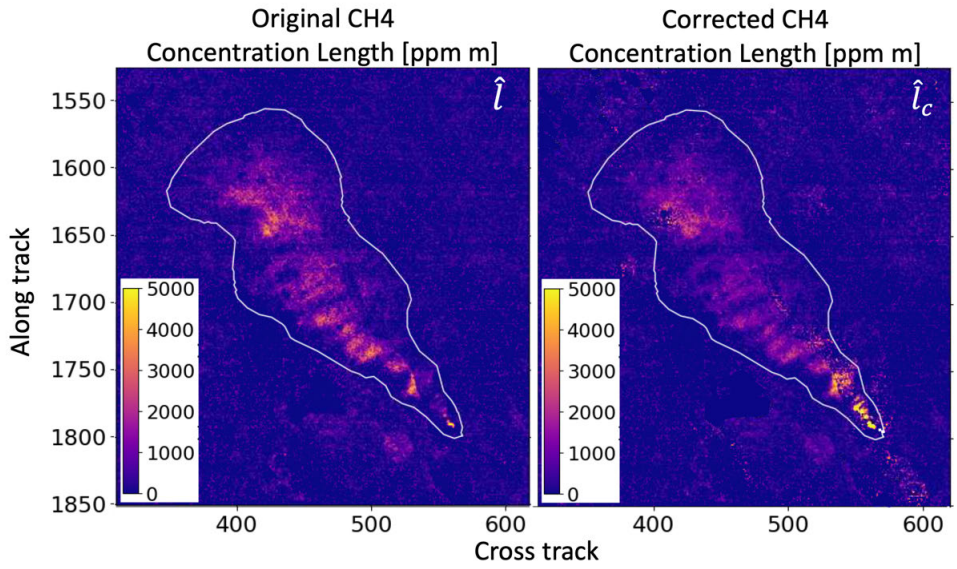

Fig. 4. (Left) Original concentration length $\hat{l}$ and (right) corrected $\hat{l}_c$ corresponding to the region shown in Fig. 3.

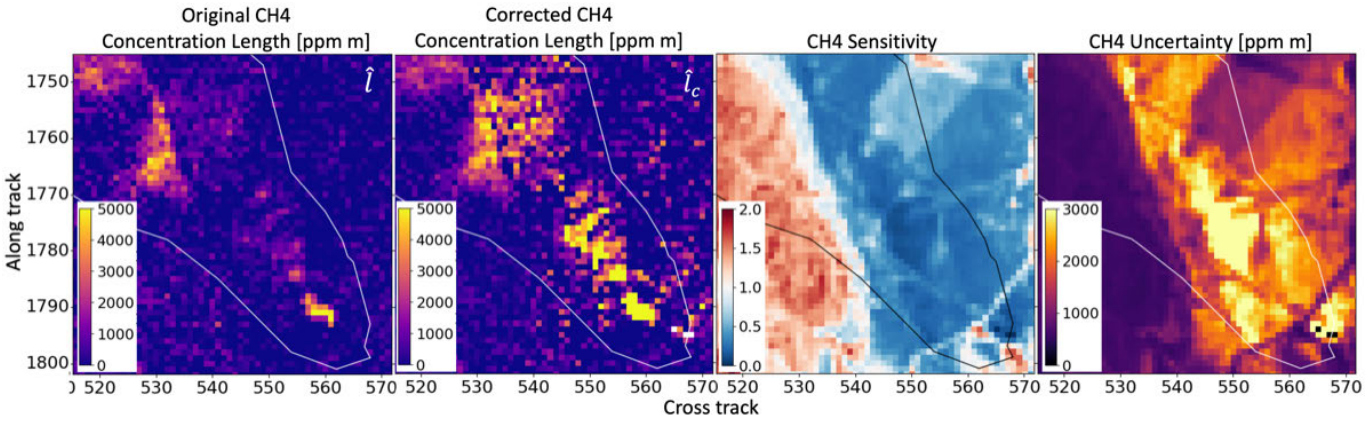

Fig. 5. From (left) Original concentration length $\hat{l}$, corrected $\hat{l}_c$, CH_4 sensitivity S, and CH_4 uncertainty U for EMIT scene emit20230612t162103 corresponding to the green box in Fig. 3.

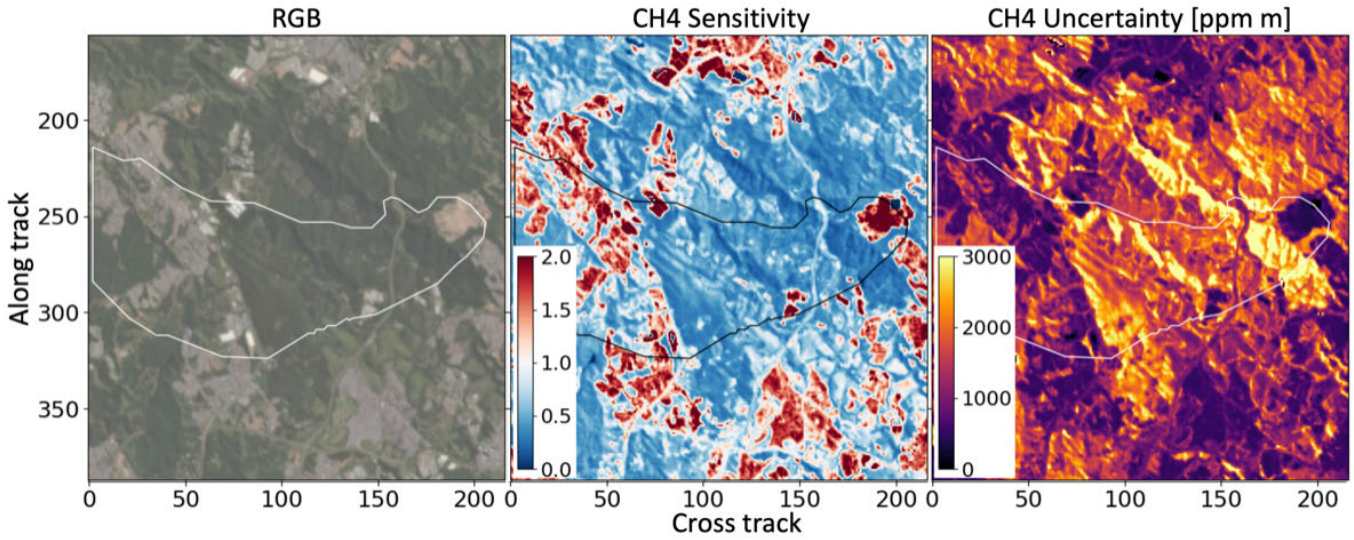

Fig. 6. From (left) RGB image of EMIT scene emit20230504t135454, CH_4 sensitivity S, and CH_4 uncertainty U.

into the estimated concentration length, the result of which is shown in the bottom panel. The middle column shows the simulated plume directly, while the second shows the simulated plume multiplied by the sensitivity to account for

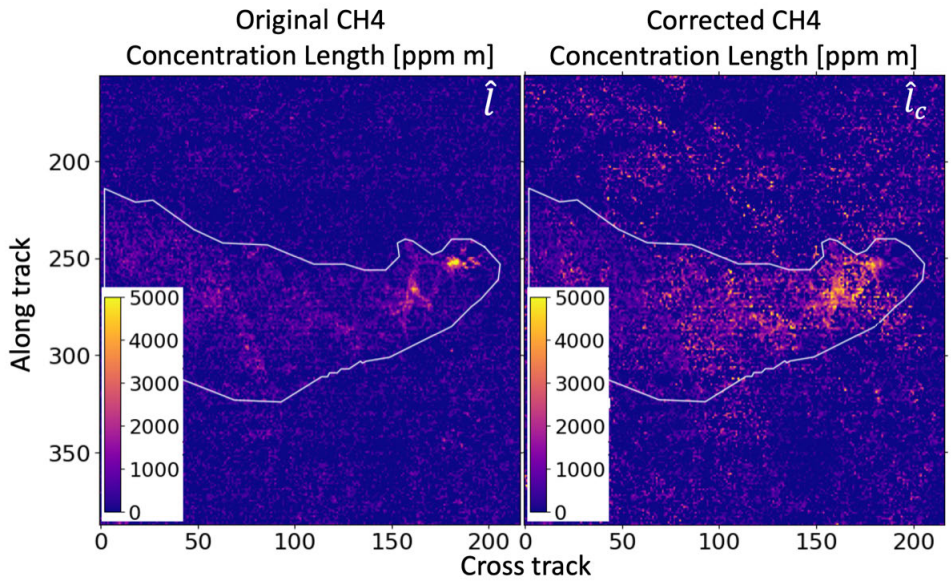

Fig. 7. (Left) Original concentration length $\hat{l}$ and (right) corrected $\hat{l}_c$ corresponding to Fig. 6.

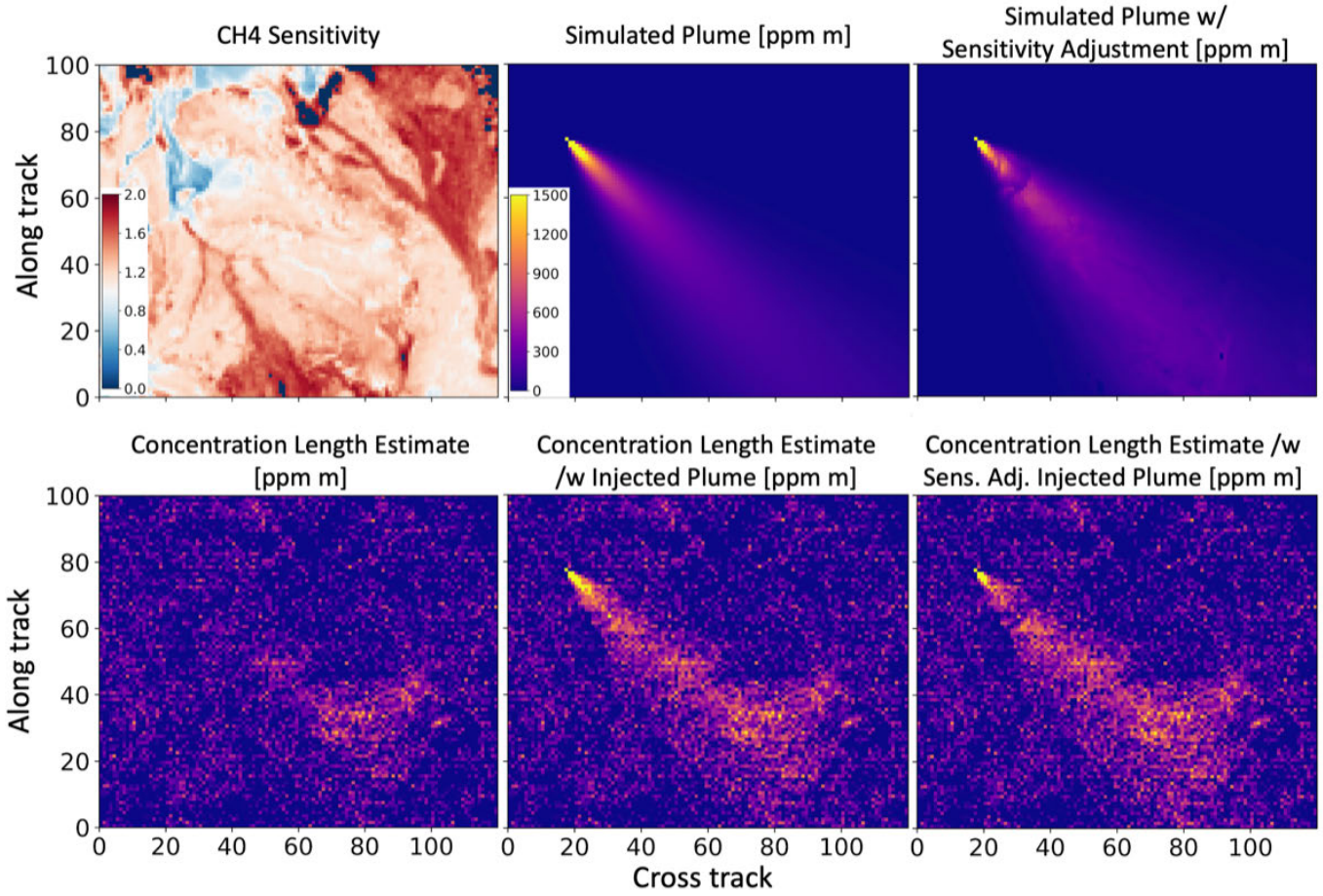

Fig. 8. Simulated plume injected into data for a region selected to have no true CH_4 plume in EMIT scene emit20220818t034231. From (left) to (right) and from (top) to (bottom) CH_4 sensitivity, simulated plume, simulated plume with the sensitivity applied, uncorrected concentration length estimate $\hat{l}$, same but with simulated plume injected, same but with sensitivity-adjusted plume injected. Note that all five plots of concentration length share the same colorscale shown in the upper middle panel. See the main text for details.

the apparent variation in the concentration length due to the scene background. The amorphous enhancement shown at (cross track, along track) pixel (80, 30) is likely not due to the actual presence of methane but more likely due to the

bias caused when κ deviates from one, as in the second term of (10). However, after the plume is injected into the scene, it becomes impossible to distinguish the background bias from the true plume. In this case, it is likely that a plume delineation method might incorrectly but inadvertently include the bulge due to the background as part of the true plume. Unfortunately, this type of bias is not addressed by the sensitivity correction and in fact, could be exacerbated by it.

IV. Discussion and Conclusion

The concentration length sensitivity and uncertainty metrics described above encapsulate several effects that are important for quantifying gas emissions. These include the concentration length bias due to surface and atmospheric variation and the statistical uncertainty due to noise. The expressions for the rms error quantify these effects in a way that may otherwise be difficult to visualize. The metrics are additionally useful to indicate a given site's potential for detecting methane in future data collections given the local surface variation and how that variation might play through to the apparent spatial distribution of a potential plume. The uncertainty provides similar information to quantify the expected statistical uncertainty. It also includes effects that tend to change the signal-to-noise ratio, including solar and look geometry. Used together, these metrics may help to identify weaker CH_4 plumes and reject surface biases in the estimator that drive false positive detections.

A. Plume Emission Rate

One application of these uncertainty and sensitivity metrics involves reducing uncertainty in the downstream estimation of plume CH_4 emission rates. Error in such estimates comes from a variety of sources, including wind speed, local meteorology, topography, and land cover type [22]. Previous studies that calculated plume emission estimates from concentration length did not incorporate a per-pixel concentration length uncertainty nor account for the bias captured in the sensitivity metric. For example, preliminary EMIT CH_4 and CO_2 integrated mass enhancement-derived emission results from a subset of 2022 EMIT acquisitions relied only on wind speed uncertainty to estimate emission uncertainties [11]. In addition, plume emission rate estimates from Airborne Visible/Infrared Imaging Spectrometer Next Generation (AVIRIS-NG) data collected during controlled release experiments derived uncertainties from windspeed and IME variability due to plume length and variable thresholding [16]. Incorporation of the sensitivity correction and the statistical uncertainty metric derived here into the emission rate calculations may help to improve accuracy by reducing biases due to local surface variation and yield improved quantification of the rate estimates' uncertainty.

B. Sensor Design

A second application of these metrics is in the domain of instrument design. Fig. 1 demonstrates how a particular instruments' noise model can translate directly to an anticipated rms error for surfaces that deviate from the mean in different amounts. This leads to the natural potential to work backward from an acceptable error in physical units (e.g., concentration length) to a particular sensor noise characterization. Notably, the use of (11) leads to an inverse correlation between albedo and error, which is what is typically observed from match filter results and expected from the literature in general [23]. This contrasts the noise model of most imaging spectrometers, which tend toward higher noise rates with higher signals [17], [24]; but does correspond to the general trend of SNR, which typically increases with brighter targets because of nonlinearity in the noise function. While previous (uncorrected) estimates of the error would lead to a complicated design choice, as per Fig. 1(a), the corrected estimator provides a quantitative means to express how increased instrument performance translates into uniform decreased error. While these estimates of performance are not comprehensive, they do provide a new best basis from which to build in the instrument design trade space.

C. Enhancing Machine Learning Retrievals

With the increasing volumes of data available for analysis, the need for automation of methods for plume detection and emissions quantification increases. Many such methods have been proposed, largely centered on some form of convolutional neural network (e.g., [25], [26]), but at the time of this writing no such system is fully deployed in an operational setting to our knowledge. This stems largely from the desire to prevent the identification of false positives, and we anticipate this changing in the coming years. Including sensitivity or uncertainty layers as inputs to such automation methods may provide a mechanism to improve the efficacy of such methods under these stringent requirements.

V. Open Science

Software implementations of the sensitivity and uncertainty metrics for the EMIT sensor are available on GitHub at https://github.com/emit-sds/emit-ghg. The EMIT-matched filter results used for the figures are available at https://lpdaac.usgs.gov/products/emitl2bch4enhv001/, while the radiance inputs are available at https://lpdaac.usgs.gov/products/emitl1bradv001/. The sensitivity and uncertainty metrics will be incorporated into the Version 002 release of the EMIT L2BCH4ENH product.

Acknowledgment

This research was carried out at the Jet Propulsion Laboratory, California Institute of Technology, under a contract with the National Aeronautics and Space Administration. Special thanks to NASA's Earth Science Division and J. Kaye for sustained support of imaging spectroscopy for greenhouse gas applications. US Government Support Acknowledged.

Author Contributions

Jay E. Fahlen: conceptualization, methodology, formal analysis, investigation, writing, and visualization. Philip G. Brodrick: EMIT product generation, methodology, writing, and revising. Red Willow Coleman: writing and revising. Clayton D. Elder: investigation and manuscript revisions. David R. Thompson: production and

refinement of EMIT radiance products, methodology, writing, and revising. Andrew K. Thorpe: methodology and writing. Robert O. Green: conceptualization, methodology, and funding acquisition. Joseph J. Green: methodology. Amanda M. Lopez: data curation and writing. Chuchu Xiang: writing.

REFERENCES

[1] D. A. Roberts, E. S. Bradley, R. Cheung, I. Leifer, P. E. Dennison, and J. S. Margolis, "Mapping methane emissions from a marine geological seep source using imaging spectrometry," *Remote Sens. Environ.*, vol. 114, no. 3, pp. 592–606, Mar. 2010.

[2] A. K. Thorpe, C. Frankenberg, and D. A. Roberts, "Retrieval techniques for airborne imaging of methane concentrations using high spatial and moderate spectral resolution: Application to AVIRIS," *Atmos. Meas. Techn.*, vol. 7, no. 2, pp. 491–506, Feb. 2014.

[3] D. R. Thompson et al., "Real-time remote detection and measurement for airborne imaging spectroscopy: A case study with methane," *Atmos. Meas. Techn.*, vol. 8, no. 10, pp. 4383–4397, Oct. 2015.

[4] A. K. Thorpe et al., "Airborne DOAS retrievals of methane, carbon dioxide, and water vapor concentrations at high spatial resolution: Application to AVIRIS-NG," *Atmos. Meas. Techn.*, vol. 10, no. 10, pp. 3833–3850, Oct. 2017.

[5] C. Frankenberg et al., "Airborne methane remote measurements reveal heavy-tail flux distribution in four corners region," *Proc. Nat. Acad. Sci. USA*, vol. 113, no. 35, pp. 9734–9739, Aug. 2016.

[6] A. K. Thorpe et al., "Mapping methane concentrations from a controlled release experiment using the next generation airborne visible/infrared imaging spectrometer (AVIRIS-NG)," *Remote Sens. Environ.*, vol. 179, pp. 104–115, Jun. 2016.

[7] D. R. Thompson et al., "Space-based remote imaging spectroscopy of the Aliso canyon CH4 superemitter," *Geophys. Res. Lett.*, vol. 43, no. 12, pp. 6571–6578, Jun. 2016.

[8] D. J. Varon et al., "Satellite discovery of anomalously large methane point sources from Oil/Gas production," *Geophys. Res. Lett.*, vol. 46, no. 22, pp. 13507–13516, Nov. 2019.

[9] L. Guanter et al., "Mapping methane point emissions with the PRISMA spaceborne imaging spectrometer," *Remote Sens. Environ.*, vol. 265, Nov. 2021, Art. no. 112671.

[10] D. J. Varon, D. Jervis, J. McKeever, I. Spence, D. Gains, and D. J. Jacob, "High-frequency monitoring of anomalous methane point sources with multispectral Sentinel-2 satellite observations," *Atmos. Meas. Techn.*, vol. 14, no. 4, pp. 2771–2785, Apr. 2021.

[11] A. K. Thorpe et al., "Attribution of individual methane and carbon dioxide emission sources using EMIT observations from space," *Sci. Adv.*, vol. 9, no. 46, Nov. 2023, Art. no. eadh2391.

[12] R. M. Duren et al., "California's methane super-emitters," *Nature*, vol. 575, no. 7781, pp. 180–184, 2019.

[13] C. D. Elder, D. R. Thompson, A. K. Thorpe, P. Hanke, K. M. Walter Anthony, and C. E. Miller, "Airborne mapping reveals emergent power law of Arctic methane emissions," *Geophys. Res. Lett.*, vol. 47, no. 3, Feb. 2020, Art. no. e2019GL085707.

[14] C. D. Elder et al., "Characterizing methane emission hotspots from thawing permafrost," *Global Biogeochemical Cycles*, vol. 35, no. 12, Dec. 2021, Art. no. e2020GB006922.

[15] A. K. Thorpe et al., "Improved methane emission estimates using AVIRIS-NG and an airborne Doppler wind LiDAR," *Remote Sens. Environ.*, vol. 266, Dec. 2021, Art. no. 112681.

[16] A. K. Ayasse, D. Cusworth, K. O'Neill, J. Fisk, A. K. Thorpe, and R. Duren, "Performance and sensitivity of column-wise and pixel-wise methane retrievals for imaging spectrometers," *Atmos. Meas. Techn.*, vol. 16, no. 24, pp. 6065–6074, Dec. 2023.

[17] D. R. Thompson et al., "On-orbit calibration and performance of the emit imaging spectrometer," *Remote Sens. Environ.*, vol. 303, 2024, Art. no. 113986.

[18] D. Manolakis, E. Truslow, M. Pieper, T. Cooley, and M. Brueggeman, "Detection algorithms in hyperspectral imaging systems: An overview of practical algorithms," *IEEE Signal Process. Mag.*, vol. 31, no. 1, pp. 24–33, Jan. 2014.

[19] D. R. Thompson, V. Natraj, R. O. Green, M. C. Helmlinger, B.-C. Gao, and M. L. Eastwood, "Optimal estimation for imaging spectrometer atmospheric correction," *Remote Sens. Environ.*, vol. 216, pp. 355–373, Oct. 2018.

[20] J. Theiler, "Absorptive weak plume detection on Gaussian and non-Gaussian background clutter," *IEEE J. Sel. Topics Appl. Earth Observ. Remote Sens.*, vol. 14, pp. 6842–6854, 2021.

[21] S. Jongaramrungruang et al., "Towards accurate methane point-source quantification from high-resolution 2-D plume imagery," *Atmos. Meas. Techn.*, vol. 12, no. 12, pp. 6667–6681, Dec. 2019.

[22] J. S. Rutherford, E. D. Sherwin, Y. Chen, S. Aminfard, and A. R. Brandt, "Evaluating methane emission quantification performance and uncertainty of aerial technologies via high-volume single-blind controlled releases," Stanford Univ., Palo Alto, CA, USA, 2023, doi: 10.31223/X5KQ0X. [Online]. Available: https://eartharxiv.org/repository/view/5113/

[23] M. D. Foote et al., "Fast and accurate retrieval of methane concentration from imaging spectrometer data using sparsity prior," *IEEE Trans. Geosci. Remote Sens.*, vol. 58, no. 9, pp. 6480–6492, Sep. 2020.

[24] J. W. Chapman et al., "Spectral and radiometric calibration of the next generation airborne visible infrared spectrometer (AVIRIS-NG)," *Remote Sens.*, vol. 11, no. 18, p. 2129, Sep. 2019.

[25] P. Joyce et al., "Using a deep neural network to detect methane point sources and quantify emissions from PRISMA hyperspectral satellite images," *Atmos. Meas. Techn.*, vol. 16, no. 10, pp. 2627–2640, May 2023.

[26] S. Jongaramrungruang, A. K. Thorpe, G. Matheou, and C. Frankenberg, "MethaNet—An AI-driven approach to quantifying methane point-source emission from high-resolution 2-D plume imagery," *Remote Sens. Environ.*, vol. 269, Feb. 2022, Art. no. 112809.

Jay E. Fahlen received the B.S., M.S., and Ph.D. degrees from the University of California at Los Angeles, Los Angeles, CA, USA, in 2001, 2004, and 2010, respectively, all in electrical engineering.

He is a Research Technologist with the Jet Propulsion Laboratory, California Institute of Technology, Pasadena, CA, USA. His research interests include spanned video processing, computational plasma physics, signal processing for both radar and imaging spectrometers and greenhouse gas detection and quantification methods using remote imaging spectroscopy.

Philip G. Brodrick received the B.S. degree in physics and the M.S. degree in renewable and clean energy systems from the University of Dayton, Dayton, OH, USA, in 2010 and 2012, respectively, and the Ph.D. degree in energy systems engineering from Stanford University, Stanford, CA, USA, in 2017.

He is a Data Scientist with the Jet Propulsion Laboratory, California Institute of Technology, Pasadena, CA, USA. His works on algorithm development and science applications for imaging spectroscopy across disciplines, ranging from advances in retrieval techniques to the interpretation of biogeophysical signals. He is currently the Project Scientist for the Earth Surface Mineral Dust Source Investigation (EMIT) and the Project Algorithm Scientist for NASA's SBG-VSWIR mission.

Red Willow Coleman received the B.S. degree in mathematical and computational biology with an emphasis in environmental analysis from Harvey Mudd College, Claremont, CA, USA, in 2022.

She is currently a Research Technologist with the Imaging Spectroscopy Group, NASA Jet Propulsion Laboratory (JPL), Pasadena, CA, USA, working with airborne and orbital imaging spectrometers. Her research interests include imaging spectroscopy, greenhouse gas detection, remote sensing, and urban environmental policy.

Clayton D. Elder received the Ph.D. degree in earth system science from the University of California at Irvine, Irvine, CA, USA, in 2018, focusing on the utilization of rare carbon isotopes to investigate the origins and scale of greenhouse gas emissions in Arctic lakes.

He is a Research Scientist within the Biospheric Science Branch, NASA Ames, Mountain View, CA, USA. As a Research Scientist at the Jet Propulsion Laboratory, Pasadena, CA, USA, and now NASA Ames, he continues his study of the changing Arctic carbon cycle and its implications for global climate. More broadly, he employs airborne and spaceborne imaging spectroscopy techniques to detect and elucidate environmental patterns of ecological and anthropogenic methane emission hotspots.

David R. Thompson (Senior Member, IEEE) is a Senior Research Scientist with the Jet Propulsion Laboratory, California Institute of Technology, Pasadena, CA, USA. He is the Deputy Project Scientist for NASA's SBG-VSWIR mission and an Instrument Scientist for NASA's EMIT and HVM3 imaging spectrometers.

Dr. Thompson has received the NASA Exceptional Technology Achievement Medal, the Lew Allen Award for Excellence, and the NASA Early Career Achievement Medal.

Andrew K. Thorpe received the B.Sc. degree in geological sciences from Brown University, Providence, RI, USA, in 2004, and the Ph.D. degree in geography with a remote sensing focus from the University of California at Santa Barbara, Santa Barbara, CA, USA, in 2015.

He is a Research Technologist with the Imaging Spectroscopy Group, Jet Propulsion Laboratory, California Institute of Technology, Pasadena, CA, USA. For over a decade, he has worked with imaging spectrometer data and developed methods for high spatial resolution mapping of methane and carbon dioxide point source emissions using imaging spectrometers like AVIRIS, AVIRIS-NG, AVIRIS-3, and EMIT. He has developed quantitative gas retrievals using differential optical absorption spectroscopy, and methods to estimate emission rates, and contributed to projects aimed at visualizing methane results and reducing data latency. He is currently an EMIT Science Team member leading the EMIT greenhouse gas mapping application and the Deputy Instrument Scientist for the Carbon Plume Mapper instrument. He is also involved in ongoing efforts to develop instrument concepts for dedicated imaging spectrometers for trace gas mapping and quantification.

Robert O. Green is the Principal Investigator of the Earth Surface Mineral Dust Source Investigation (EMIT) a state-of-the-art imaging spectrometer on the International Space Station, and for AVIRIS with more than 35 000 Google Scholar results. He was the Instrument Scientist for the NASA Moon Mineralogy Mapper (M3) that discovered water/hydroxyl on the illuminated surface of the Moon. He is a science Co-Investigator and Instrument Scientist on the Mapping Imaging Spectrometer for Europa (MISE) and a science Co-Investigator on the NASA Lunar Trailblazer mission to investigate volatile compounds and minerals on the Moon. At JPL, Pasadena, CA, USA, he is the Instrument Scientist for the Carbon Plume Mapper imaging spectrometer to measure and mitigate sources of methane. He is a Senior Research Scientist, JPL Fellow, and Director of the Microdevices Laboratory. For more than 25 years, his research has used remote measurement via imaging spectroscopy to test hypotheses and pursue scientific investigations and applications on Earth and for discovery through the solar system.

Joseph J. Green has been at the forefront of advancements in wavefront sensing and control, active optics, high-contrast imaging, and image and spectroscopic data analysis for the past 24 years. He has made significant contributions to astrophysics and planetary and earth science missions, including JWST, Spitzer, and Mars Perseverance. He currently serves as the Supervisor for the Instrument Calibration and Analysis Group, Instruments Division, JPL, Pasadena, CA, USA.

Dr. Green was a member of the team that won the NASA Software of the Year Award for its Adaptive MGS Wavefront Sensing software, in 2007. He received JPL's top awards for Technical Excellence in 2008 and Technical Leadership in 2017 for his work supporting Non-NASA Government efforts.

Amanda M. Lopez received the Ph.D. degree in geology from the University of Houston, Houston, TX, USA, in 2021.

She is a Geoscience Researcher with NASA Jet Propulsion Laboratory, Pasadena, CA, USA, and the UCLA Joint Institute for Regional Earth System Science and Engineering. Her research interests include understanding the impact of wildfires on watersheds and coastal environments and identifying point source greenhouse gas emissions using geographic information systems (GIS), watershed modeling, and remote sensing. She explored the biogeochemical cycling of trace metal contaminants in the Galveston Bay estuary gaining experience with isotope geochemistry, analytical chemistry, and mass spectrometry. She has additional experience in environmental consulting, marine renewable energy, and science education. Outside of work she enjoys board games, tennis, a fresh pot of tea, and her curmudgeonly cat.

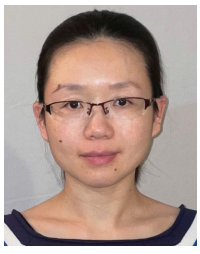

Chuchu Xiang received the Ph.D. degree from Baylor University, Waco, TX, USA, in 2019.

She is a Post-Doctoral Researcher with the Jet Propulsion Laboratory, California Institute of Technology, Pasadena, CA, USA. Her doctoral and post-doctoral work concentrated on modeling and data analysis of dust coagulation and chondrule dust rim formation in protoplanetary disks at Baylor University. Her research interests include the automatic identification of false positive methane plumes for orbital imaging spectrometers.